Physisorption-Based Charge Transfer in Two-Dimensional SnS_2 for Selective and Reversible NO_2 Gas Sensing

Jian Zhen Ou,*,† Wanyin Ge,‡ Benjamin Carey,† Torben Daeneke,† Asaf Rotbart,† Wei Shan,‡ Yichao Wang,† Zhengqian Fu,§ Adam F. Chrimes,† Wojtek Wlodarski,† Salvy P. Russo,*,∥ Yong Xiang Li,*,†,‡,§ and Kourosh Kalantar-zadeh*,†

†School of Electrical and Computer Engineering, RMIT University, Melbourne, VIC 3000, Australia, ‡The Key Laboratory of Inorganic Functional Materials and Devices, Shanghai Institute of Ceramics, Chinese Academy of Sciences, 200050 Shanghai, P.R. China, §School of Physical Science and Technology, ShanghaiTech University, 200031 Shanghai, P.R. China, and ∥School of Applied Sciences, RMIT University, Melbourne, VIC 3000 Australia

ABSTRACT Nitrogen dioxide (NO_2) is a gas species that plays an important role in certain industrial, farming, and healthcare sectors. However, there are still significant challenges for NO_2 sensing at low detection limits, especially in the presence of other interfering gases. The NO_2 selectivity of current gas-sensing technologies is significantly traded-off with their sensitivity and reversibility as well as fabrication and operating costs. In this work, we present an important progress for selective and reversible NO_2 sensing by demonstrating an economical sensing platform based on the charge transfer between physisorbed NO_2 gas molecules and two-dimensional (2D) tin disulfide (SnS_2) flakes at low operating temperatures. The device shows high sensitivity and superior selectivity to NO_2 at operating temperatures of less than 160 °C, which are well below those of chemisorptive and ion conductive NO_2 sensors with much poorer selectivity. At the same time, excellent reversibility of the sensor is demonstrated, which has rarely been observed in other 2D material counterparts. Such impressive features originate from the planar morphology of 2D SnS_2 as well as unique physical affinity and favorable electronic band positions of this material that facilitate the NO_2 physisorption and charge transfer at parts per billion levels. The 2D SnS_2-based sensor provides a real solution for low-cost and selective NO_2 gas sensing.

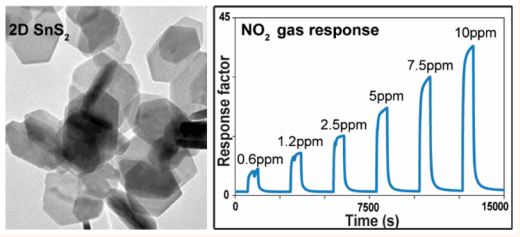

KEYWORDS: two-dimensional materials · post-transition metal dichalcogenide · SnS_2 · gas sensor · nanosheet · physisorption

Nitrogen dioxide (NO_2) is an industrially and biologically important gas species, which can be particularly dangerous to humans at levels greater than 1 ppm, causing damage to the respiration system and worsening respiratory diseases.[1,2] The United States environmental protection agency recognizes NO_2 as an air pollutant that is co-released during many types of fuel combustions.[3] It plays an important role in the chemistry of the atmosphere, producing acid rain and contributing to the formation of ozone (O_3), which is the major cause of photochemical smog.[4] NO_2 is also an important material for the synthesis of nitric acid that is used in the production of fertilizers for agriculture and explosives for both military and mining uses.[5] Furthermore, NO_2 is an essential gas for many biosystems. Nitrogen monoxide (NO) appears as a gasotransmitter in many cell-signaling pathways,[6] which can convert to NO_2 rapidly when exposed to an environmental disturbance in the presence of oxygen. The sensing of nitrogen oxides (NOx, a group mainly consisting of NO_2 and NO) can be potentially implemented in diagnostic processes. For instance, the detection of NOx in exhaled breath (at parts per billion (ppb) levels) is helpful for identifying infections of lung tissues.[7] In addition, the NOx can possibly be used as a biomarker for some of the gastrointestinal disorder symptoms such as irritable bowel disease.[6]

It is important to consider that in many of the aforementioned sensing scenarios, NO_2 gas should be measured in the presence of other interfering gas species. Therefore, the realization of accurate, highly selective, and low detection limit NO_2 gas sensors, which can operate in a wide range of ambient conditions, is a critical step in environmental monitoring and surveillance in many industries as well as healthcare and clinical practices.

* Address correspondence to jianzhen.ou@rmit.edu.au, slavy.russo@rmit.edu.au, yongxiang.li@rmit.edu.au, kourosh.kalantar@rmit.edu.au.

Received for review July 14, 2015 and accepted October 8, 2015.

Published online October 08, 2015
10.1021/acsnano.5b04343

Based on the sensing mechanism, the current NO_2 gas sensor technologies can be mainly categorized into optical, electrochemical, and chemiresistor types.[8] Optical methods predominately rely on the unique optical fingerprints of NO_2 gas molecules, including their chemiluminescent emission and infrared light absorption wavelengths, which result in high-selectivity NO_2 sensing. Such optical sensing methods need sophisticated instruments or system configurations to achieve a high NO_2 sensitivity, which significantly increase their sizes and costs.[8−12] Instead, electrochemical sensing of NO_2, which relies on the electrochemical reduction of NO_2 in the presence of noble catalysts, is a low-cost approach.[13] Nevertheless, such sensors have cross-talk with active gas species such as hydrogen, and their operation lifetimes are relatively short.[14] These drawbacks can be increasingly eliminated by using zirconia-based solid electrolytes.[15] However, their high operation temperatures (in the range of 500−900 °C) result in significant operation costs and limit their applications mostly to combustion and automotive monitoring systems. Another economical method of NO_2 sensing is based on chemiresistor transducing platforms, relying on the charge transfer between metal oxides and surface chemisorbed NO_2.[16,17] However, the pristine or modified surface of these metal oxides shows weak discrimination to different gas species, making them poorly selective. Furthermore, the presence of oxygen is crucial for the operation of chemiresistive metal oxide compounds, which is not suitable for some particular anaerobic applications. Finally, high operation temperature above 200 °C is needed in order to improve the response and recovery kinetics of these sensors.

Therefore, considering the trade-offs between sensitivity, selectivity, and cost, there still exists an ongoing quest for the ideal NO_2-sensing platform. The paramagnetic nature of NO_2 can be utilized to realize a different class of highly selective NO_2 gas sensors, as it can produce a magnetic dipole in addition to a surface electric dipole generated by the mirror charge when it is physisorbed onto the surface of a sensitive layer, resulting in a much stronger affinity compared to other nonmagnetic gases such as CO_2, H_2, H_2S, and CH_4.[18] Upon the NO_2 molecule adsorption, a charge transfer can occur depending on the relative band positions of sensitive material and NO_2 as well as possible hybridization of gas molecule states with sensitive material orbitals.[19,20] Such a charge transfer affects the electrical resistance of the sensitive material, which can be facilely measured using the low-cost resistive transducing platform. More importantly, the physisorption of gas molecules can occur at low temperatures, and the corresponding charge transfer mechanism does not rely on the breakdown of the adsorbed gas, presenting an ideal NO_2-sensing platform that can operate reliably at relatively low temperatures, regardless of the presence of ambient oxygen.

So far, the search for exploring suitable sensitive materials for selective NO_2 physisorptive sensing with high adsorption/desorption kinetics has resulted in limited success. Low-dimensional carbon-based materials, including carbon nanotubes and graphene, have been investigated as possible candidates.[21−24] Although excellent sensitivities toward NO_2 have been demonstrated, these sensors exhibit low selectivity and slow recovery kinetics.[25] The emergence of two-dimensional (2D) transition metal dichalcogenides (TMDs)[26−30] and phosphorene[31,32] as the alternatives has alleviated some of these drawbacks, but the outcomes are still far from sufficient practical values. Especially, the most prominent candidate to date, 2D molybdenum disulfide (MoS_2), despite presenting a good selectivity to NO_2, does not show sufficiently fast recovery kinetics. Therefore, the realization of a low-cost sensing platform with strong potentials of excellent NO_2 physisorptive selectivity, sensitivity, and reversibility, which can operate at relatively low temperatures at a small development cost, is pending the discovery of an appropriate candidate material with a favorable surface energy value for NO_2 adsorption as well as optimum electronic band structure facilitating the charge transfer.

Although tin (Sn) does not belong to the transition metal family, tin disulfide (SnS_2) exists in a layered crystal phase,[33] which is similar to TMDs in various aspects.[34,35] This phase is composed of Sn atoms sandwiched between two layers of hexagonally disposed close packed sulfur (S) atoms; the adjacent S layers are connected by the weak van der Waals forces (Figure 1a). Compared to 2D MoS_2, SnS_2 has a larger electronegativity, potentially enhancing gas adsorption sites.[36] Furthermore, the relatively stronger temperature dependency on the electronic band structure of SnS_2 can possibly enable the optimization of sensing response and be used for enhancing recovery kinetics at a range of moderately elevated temperatures, advantageous for practical gas-sensing applications.[37,38]

In this work, we present a novel approach for selective and reversible NO_2 gas sensing based on 2D SnS_2 flakes. Many of the current synthesis methods of 2D SnS_2 are based on exfoliation, wet chemical, and vapor deposition techniques.[39−45] Here, the planar 2D SnS_2 flakes are synthesized *via* a facile wet chemical route. The planar few-layered 2D structure is selected as it both provides large active surface area for more efficient adsorption of NO_2 gas molecules and also facilitates their accommodation into the van der Waals spacing due to small SnS_2 interlayer binding energy (∼10−20 meV/Å^2).[46] We show that these 2D SnS_2 flakes are integrated onto low-cost resistive transducing platforms for highly selective and exceptionally

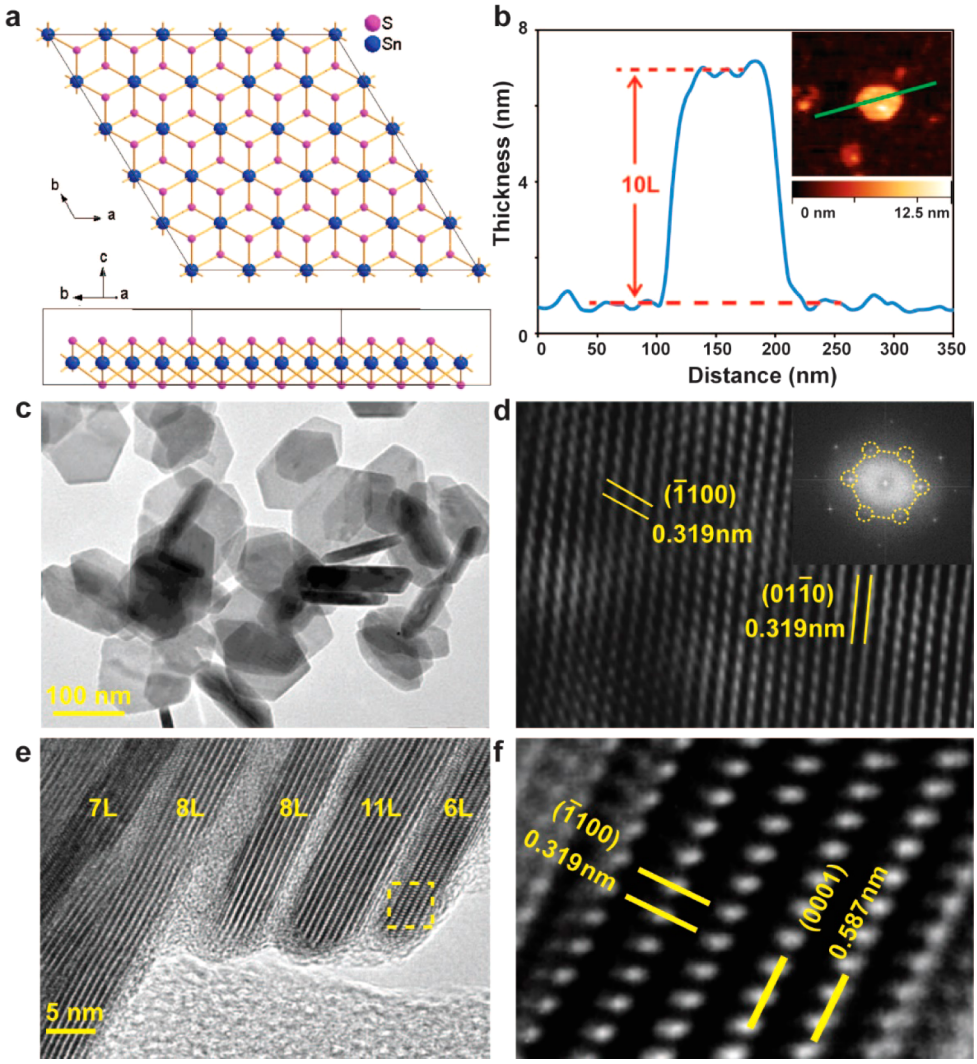

Figure 1. Morphological and structural characterization of 2D SnS_2 flakes. (a) Top and cross-sectional schematics of SnS_2. (b) Height profile of a typical 2D SnS_2 flake along the green line in the AFM image inset. (c) TEM image of 2D SnS_2 flakes. (d) HRTEM image of a typical 2D SnS_2 flake. (e) Cross-sectional HRTEM of 2D SnS_2 flakes. (f) Zoomed-in HRTEM figure indicating that the interlayer spacing for hexagonal SnS_2 is 0.587 nm.

sensitive NO_2 gas sensing at ppb levels, which relies on the physisorption-based charge transfer.

RESULTS AND DISCUSSION

The 2D SnS_2 flakes were prepared by a wet chemical synthesis technique (details are presented in the Materials and Methods section). In brief, upon the mixture of Sn precursor and sulfurization reagents at elevated temperatures, the preferential crystal nucleation occurs at the lateral planes due to the strong coupling along them. The existence of excessive dangling bonds at the edges causes the growth of SnS_2 crystals to be continued with a high anisotropic nature, resulting in the planar 2D morphology. Atomic force microscopy (AFM) verifies the presence of 2D hexagonal flakes with thicknesses on the order of multiple SnS_2 unit cells in the as-synthesized flakes. A typical example is the AFM image shown in Figure 1b, which is a ~6 nm thick 2D flake corresponding to 10 monolayers of SnS_2, as the thickness of a monolayer of SnS_2 is ~0.59 nm.[39,41] A statistical analysis based on AFM measurements indicates that the 2D flakes have different thicknesses, with the majority lying in the range of 7−11 monolayers (Figure S1a). The obtained hexagonal 2D flakes demonstrate some polydispersity in lateral dimensions mainly ranging from 80 to 200 nm according to the transmission electron microscopy (TEM) imaging and dynamic light scattering (DLS) pattern shown in Figures 1c and S1b, respectively. Figure 1d shows the high-resolution TEM (HRTEM) image of a 2D SnS_2 flake, in which a lattice fringe spacing of 0.319 nm is identified and corresponds to both the $(\bar{1}100)$ and $(01\bar{1}0)$ lattice planes of hexagonal SnS_2. The inset in Figure 1d presents the fast Fourier transform (FFT) pattern of this region, showing the faceted edges with an angle of 120°, which corresponds to the hexagonal symmetry of crystalline SnS_2 projected along the *c*-axis. The cross-sectional HRTEM

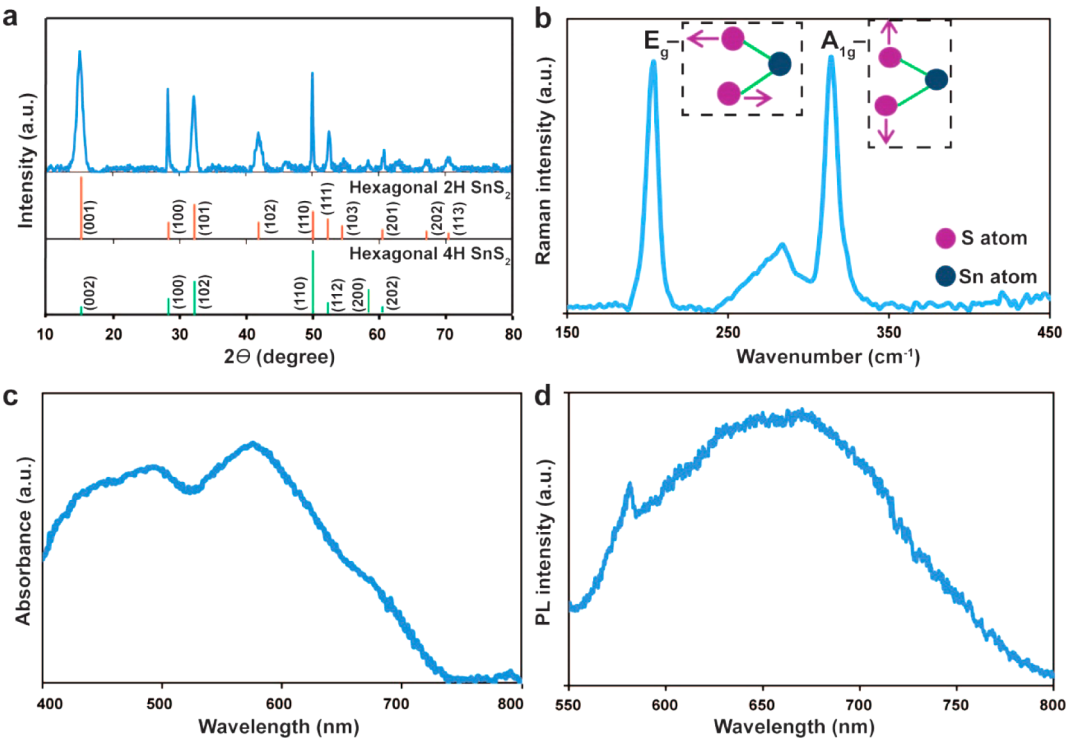

Figure 2. Crystal structure and optical properties of 2D SnS_2 flakes. (a) XRD pattern of 2D SnS_2 flakes. (b) Raman spectrum of 2D SnS_2 flakes at a laser excitation wavelength of 785 nm with schematics of E_g and A_{1g} Raman vibrational modes. (c) Optical absorption spectrum of 2D flakes at the wavelengths between 400 and 800 nm. (d) Photoluminescence spectrum of 2D flakes at an excitation wavelength of 532 nm.

image illustrated in Figure 1e confirms that these 2D SnS_2 flakes consist of an average of 9 ± 2 layers with an interlayer distance of 0.587 nm (Figure 1f).

X-ray diffraction (XRD) assessment was utilized to further investigate the crystal phase of 2D hexagonal SnS_2 flakes. From Figure 2a, the primary diffraction peaks of 2D flakes at 15.04, 28.27, 32.17, 41.95, 50.05, 52.45, and 60.62° are ascribed to the (001), (100), (101), (102), (110), (111), and (201) planes, respectively, which are in accordance with the hexagonal 2H SnS_2 structure (ICDD 23-0677). The 2H SnS_2 belongs to the space group $P\bar{3}m1$ and has three atoms in the unit cell, which extend over only one monolayer.[47] However, the additional appearance of a small diffraction peak at ~58° and the relatively intensified peak at 50.05° suggest the coexistence of another SnS_2 crystal phase, which can be identified as a 4H structure (ICDD 21-1231). Although it is still within the hexagonal domain, the space group of 4H SnS_2 is changed to $P6_3mc$, which contains six atoms in a single unit cell and extends over two monolayers.[47] It is found that its composition is almost equal to that of the 2H phase when the reaction time is shortened (Figure S2), suggesting that this additional phase might be an intermediate phase during the chemical reaction.

The concurrent phase phenomenon can also be investigated by Raman spectroscopy. From Figure 2b, two distinguished Raman peaks can be found at ~205 and ~314 cm^{-1}, and there is a broad peak centered at ~288 cm^{-1} for the 2D SnS_2 flakes. The 314 cm^{-1} peak can be ascribed to the vertical plane vibration mode (A_{1g}) of Sn−S bonds of 2H SnS_2.[39,47] Nevertheless, this peak can also be contributed to the $A_1 + E$ vertical vibration Raman mode of the 4H structure due to the close position between these two structures (~313.5 cm^{-1} for the 4H structure *vs* ~314 cm^{-1} for the 2H structure[39,47]). Instead, the in-plane vibrational E mode allows a facile discrimination between 2H and 4H structures. TheE_g mode of the 2H structure appears as a single and intense band at 205 cm^{-1}, whereas the E mode of the 4H structure gives rise to a doublet at 200 and 214 cm^{-1} according to previous literature.[39,47] Therefore, the composition of the 4H structure in the 2D SnS_2 flakes is minor. The broad peak centered at 288 cm^{-1} may also be ascribed to the A_{1g} Raman mode of the 2H SnS_2, as a previous report shows that it is merged in the prominent A_{1g} mode centered at 314 cm^{-1}.[39] However, the position of this peak is overlapped with that of the B_{2g} Raman mode of SnS.[48,49] The X-ray photoelectron spectroscopy (XPS) results in Figure S3a show that there is no Sn^{2+} signature in the 2D SnS_2 flakes, indicating that the amount of SnS in the flake is negligible.

The optical properties of the 2D flakes were studied by measuring their absorption spectrum (Figure 2c). An absorption peak at ~580 nm with the shoulder centered at ~660 nm can be observed, which is ascribed to the indirect excitonic transition from the

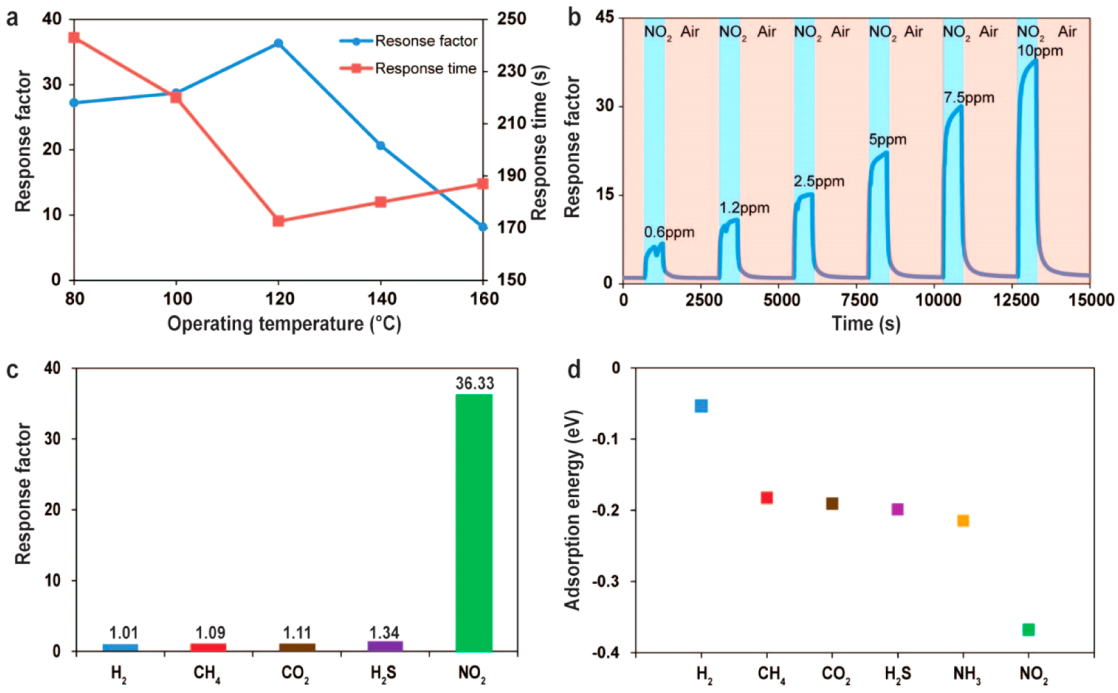

Figure 3. Gas-sensing performance of 2D SnS_2 flakes. (a) Response factor and response time of sensors made of 2D SnS_2 flakes in the presence of 10 ppm of NO_2 in synthetic air balance as a function of operation temperatures. (b) Dynamic sensing performance of 2D SnS_2 flakes toward NO_2 gas at concentrations ranging from 0.6 to 10 ppm under the operation temperature of 120 °C. (c) Measured cross-talk of 2D SnS_2 flakes toward H_2 (1%), CH_4 (10%), CO_2 (10%), H_2S (56 ppm), and NO_2 (10 ppm). (d) Calculated molecule–surface adsorption energies of 2D SnS_2 flakes toward the aforementioned gases together with NH_3.

Γ to the M point of the Brillouin zone in 2H and 4H SnS_2 structures, respectively.[50] The broad peak centered at ~490 nm can be the convoluted peak of the direct excitonic transition at the M point for both 2H and 4H structures according to a previous measurement (~484 nm for 2H and ~510 nm for 4H)[51] and theoretical calculation values (~443 nm for 2H and ~454 nm for 4H).[50] The corresponding photoluminescence (PL) spectrum of 2D SnS_2 flakes was investigated at the excitation wavelength of 532 nm. From Figure 2d, a relatively sharp peak at ~580 nm is observed, which is consistent with the position of an indirect excitonic peak of 2H SnS_2. It should be noted that the position is also close to that of SnO_x.[52] However, the XPS analysis presented in Figure S3 indicates that there is no observable coexisting SnO_x in the 2D SnS_2 flakes. The broad peak centered at ~660 nm can be ascribed to the hot PL of the indirect exciton recombination of 4H SnS_2. Although such a broad peak has been ascribed to the PL that originated from the structural impurities by a number of researchers,[53,54] the energy-dispersive X-ray (EDX) survey spectrum in Figure S4a together with the XRD pattern in Figure 2a shows no observable structural impurities in 2D SnS_2 flakes. In addition, the measured Sn/S composition ratio is ~1:2, matching the theoretical value of SnS_2, implying that the influence of substoichiometric levels and sulfur vacancies toward the electronic and optical properties of the flakes can be neglected. The mapping images of Sn and S elements displayed in Figure S4b demonstrate that both Sn and S distribute uniformly along the flake.

The 2D SnS_2 gas sensors were fabricated by drop-casting the solution containing 2D SnS_2 flakes on the resistive transducing substrates, which were made of alumina with surface interdigitated electrode (IDE) patterns (specification was presented in the Materials and Methods section). The IDE metal was chosen to ensure that Ohmic contacts were formed with drop-casted SnS_2. The electrical resistance of the device was measured for calculating the gas response factor using R_g/R_a for $R_g > R_a$ or R_a/R_g for $R_g < R_a$, where R_a and R_g represent the resistance of the device to air and the analyte gas, respectively. The sensor response and recovery time are defined as the time required for a 90% change in the full magnitude change of the gas response factor.

We tested the operation temperature of sensors from room temperature to 160 °C. For the temperatures less than 80 °C, the device did not show acceptable response/recovery time, and additionally, R_g was relatively large and beyond the measurement range of the ohm-meter. There is an observable transition from SnS_2 to tin oxide compounds (SnO_x) when the operation temperature exceeds 160 °C (Figure S5), and therefore, operation at such elevated temperatures is ruled out.

From Figure 3a and Table S1, after exposure to 10 ppm of NO_2 in synthetic air balance at the operation temperature of 80 °C, the sensor's resistance is

impressively ~28 times larger than that of only synthetic air (this translates into the initial response factor of ~28). As will be fully discussed later, the surface-adsorbed NO_2 gas molecules act as electron acceptors to receive electrons from 2D SnS_2 flakes. Such charge transfers reduce the number of free electrons in the flakes, increasing the resistance. With the increase of the operating temperature, the response factor is enhanced while the response and recovery times are decreased, suggesting that the increase of the temperature facilitates the adsorption of NO_2 gas molecules onto the 2D SnS_2 surface and enhances the charge transfer. The optimal sensing takes place at 120 °C with a maximum response factor of ~36, with the shortest response and recovery time of ~170 and ~140 s, respectively. With a further increase in the operating temperature beyond 120 °C, the response factor is dramatically dropped and the response time is slightly increased, implying that the surface desorption process of NO_2 gas becomes a more dominant effect at such temperatures.

The dynamic performance of the sensor toward NO_2 gas with concentrations ranging from 0.6 to 10 ppm at the optimum operation temperature of 120 °C is shown in Figure 3b. With the increase in the concentration of NO_2, more surface dipoles are formed before the NO_2 coverage reaches its maximum, resulting in more electron transfer from SnS_2 to NO_2. The measured response factor of the sensor is observed to be almost linear with the exposure concentrations of NO_2 gas, while the response time is greatly decreased when increasing the NO_2 concentration from 0.6 to 1.2 ppm and reaches the saturation stage afterward (Table S2). Excellent sensor reversibility is observed (Figure 3b and Figure S6) with a recovery time of less than 180 s at the optimum operating temperature regardless of the NO_2 concentration. This remarkable reversibility is not commonly seen in physisorptive charge-transfer-based sensors, and the recovery time of such systems can be up to several orders of magnitude longer due to their slow recovery kinetics.[22] Based on the NO_2 dynamic responses, the NO_2 detection limit of our sensor is estimated to be ~20−30 ppb at a noise level of ±5%. Such a low detection limit is superior in comparison to those of low-cost NO_2 optical and electrochemical sensors, which are both only in the ppm ranges,[9,12,13,15] and comparable to those of best-reported metal-oxide-based chemisorptive gas sensors (10−50 ppb),[16] which are not NO_2-selective. The value is also close to those of 2D MoS_2-[28] and carbon-based[22] physisorptive gas sensors, which show poor reversibility.

The 2D SnS_2 flakes are very strongly selective to NO_2 as only minimal responses toward other gases under investigation in this work are observed. At 120 °C, which is the near optimal operating temperature for all of those gases, response factors at industrially meaningful concentrations for H_2 (1%), CH_4 (10%), CO_2 (10%), and H_2S (56 ppm) are found to be ~1.0, ~1.1, ~1.1, and ~1.3, respectively, in comparison to ~36 for NO_2 (10 ppm) (Figure 3c). The particular selected concentrations of toxic NO_2 (10 ppm) and H_2S (56 ppm) gases are well below the immediately dangerous to life or health (IDLH) values defined by U.S. National Institute for Occupational Safety and Health (NIOSH), which are 20 and 100 ppm, respectively.[55] The exposure limit of NO_2 defined by NIOSH is recommended to be 1 ppm.[55] If this is taken into account, the NO_2 selectivity of this sensor is still superior as its response factor is ~10 at 1.2 ppm of NO_2, which is almost an order of magnitude higher than that of other aforementioned gases. In addition, the humidity plays a negligible role in the NO_2-gas-sensing performance of the sensor (Figure S7). It has also been previously shown that the response of nanostructured SnS_2 toward several other gases is relatively smaller than that of NO_2 shown here. For instance, NH_3 has a response of only ~1.5 at a concentration of 100 ppm.[56]

To understand the selectivity of 2D SnS_2 flakes toward NO_2 gas, we calculated the molecule−surface binding energies using density functional theory (DFT) to assess the dispersion forces. The outcomes are shown in Figure 3d and Table S3. The closest distance between the molecules and the surface, for the bound gas species, ranges from 2.17 to 2.87 Å, which is within the typical range for physisorbed molecules. The values of the binding energies also indicate that the physisorption occurs between the molecule and the surface for CH_4, CO_2, H_2S, NH_3, and NO_2, with NO_2 being the most strongly bound species. The binding energy for NO_2 is approximately 140 meV greater than that of the next most bound species (NH_3), while H_2 and O_2 are nonbinding due to their small adsorption energy (~50 meV) and positive adsorption energy (Table S3), respectively. The repelling of O_2 molecules on the SnS_2 surface possibly indicates that the charge transfer to the physisorbed NO_2 molecules does not rely on the presence of O_2 gas, which is distinctly different from those of metal-oxide-based chemisorptive NO_2 sensors.[16,17] The calculated surface binding energies toward different gas molecules are in accordance with the measurement results, confirming that the impressive selective NO_2 gas response of 2D SnS_2 flakes originates from its unique physical surface affinity to the gas molecules.

Another possible reason can be attributed to the influence of different gas molecules on the SnS_2 electronic band structure. Figure 4 shows the spin-resolved plots of the electronic density of states (eDOS) for the clean SnS_2 surface and for surfaces onto which aforementioned gas molecules are physisorbed. For the most weakly bound gas species (CO_2 and CH_4), the total eDOS and the projected eDOS of the nearest-neighbor surface S atoms are almost the same as for the clean surface

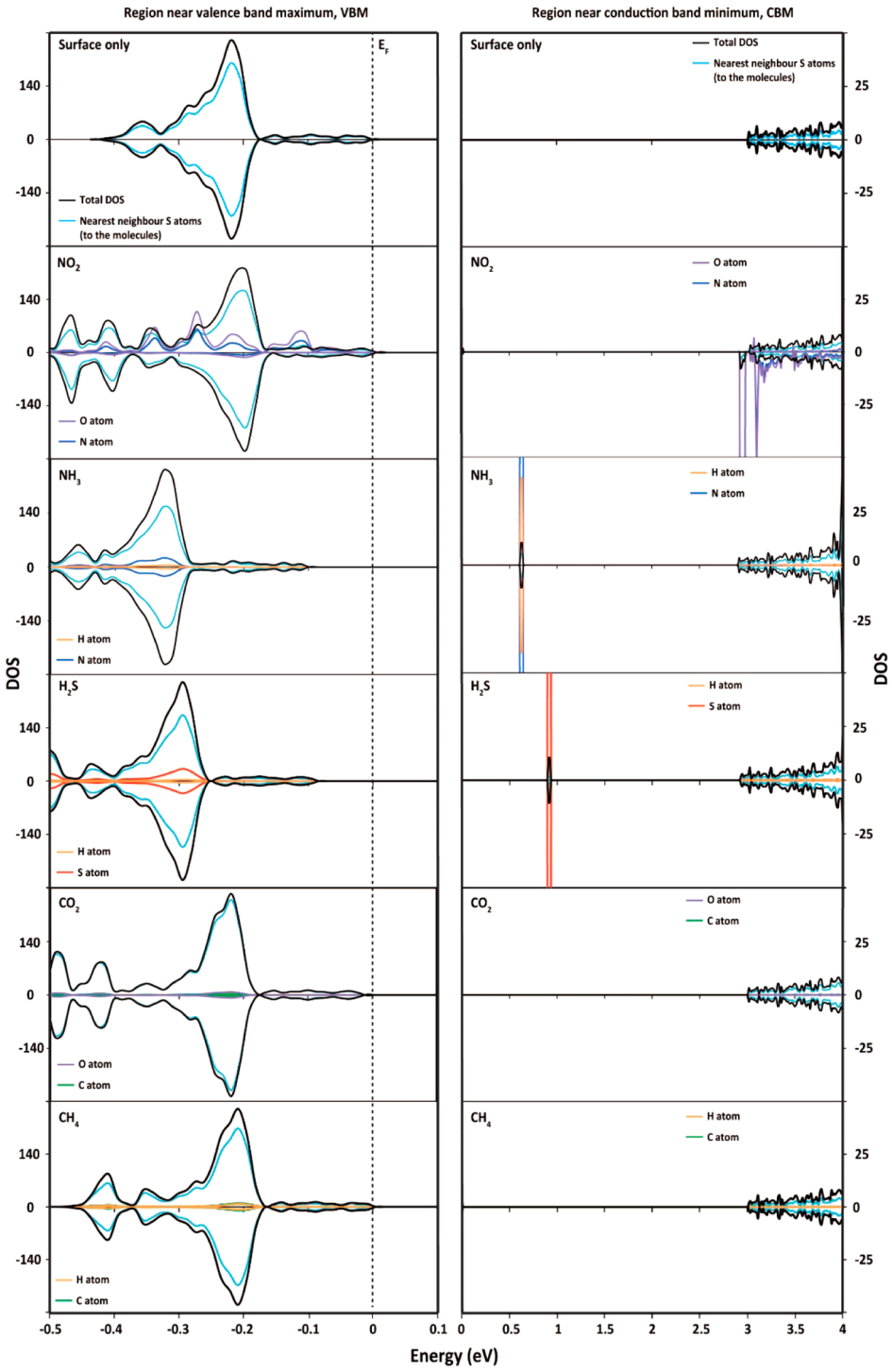

Figure 4. eDOS of NO_2, NH_3, H_2S, CO_2, and CH_4 adsorbed on SnS_2 in a 5 × 5 × 1 supercell, in which the clean surface of SnS_2 is utilized as the reference. The Fermi level (0 eV along the energy scale) is aligned to that of SnS_2 clean surface (E_F), and the total eDOS is also scaled so that the shape of the DOS can be visible on the same axis as the projected eDOS results.

near the Fermi level, suggesting that there is negligible charge transfer between the molecules and the surface. The next most bound species, H_2S and NH_3, display similar features in the eDOS. In both cases, molecular physisorption introduces states in the gap, and the projected eDOS indicates that both molecule and surface atom states contribute to this state in the band gap. In addition, the bands near the valence band maximum are shifted down by nearly 0.1 eV compared to that of the clean surface. However, these generated gap states are relatively far away from the Fermi level (~0.5−1 eV), resulting in inefficient charge transfer between the physisorbed gas molecules and the SnS_2 surface. In contrast, the eDOS for NO_2 physisorption is different from that of the other species. First, the DOS is asymmetric when comparing spin-up and spin-down,

possibly due to the formation of a surface magnetic moment upon the physisorption of NO_2 gas molecules. More importantly, while the energy bands near the conduction band minimum are lowered by ~60 meV, the band states close to the Fermi level are raised in energy by approximately 20 meV compared to the clean surface, indicating significant charge transfer from SnS_2 to the physisorbed NO_2 gas molecules.

In comparison to other 2D semiconductors, it is noted that the response factor of 2D SnS_2 toward NO_2 is at least one order larger than that of exfoliated 2D MoS_2 at a similar exposure concentration and operation temperature.[28] This can be mainly ascribed to the larger NO_2 adsorption energy of SnS_2 compared to that of MoS_2 (~150 meV),[57] resulting in more adsorption of NO_2 gas molecules either on the surface or possibly within the van der Waals gap of SnS_2 through efficient intercalation as few-layered SnS_2 has an interlayer binding energy much weaker than that of MoS_2.[46] In addition, the Mulliken population analysis of the charge density for the NO_2 physisorption indicates a transfer in charge density of 0.048 e^- from the SnS_2 surface to the NO_2 molecule, while only 0.034 e^- is observed for that of MoS_2.[57] Such an improvement can be possibly due to a more favorable Fermi energy of SnS_2 related to partially occupied molecular orbitals (POMO) of NO_2 (Figure 4), which is also another key factor for the strength of physisorption-based charge transfer.

We observed that our 2D SnS_2 sensor demonstrates a rate of NO_2 recovery kinetics much higher compared to those of previous physisorption-based sensors made of 2D materials (*e.g.*, 2D MoS_2) at elevated temperatures.[26−28] It is found that NO_2 gas molecules are favorably absorbed on the S atoms of SnS_2 with a calculated bond length of 2.41 Å, while the NO_2 gas molecules are adsorbed onto Mo atoms of MoS_2 between two sandwiched S layers with a much shorter bond length of 1.21 Å.[57] Therefore, the thermal vibration energy available at an elevated temperature causes a more efficient NO_2 gas desorption from SnS_2 compared to MoS_2. The stronger temperature dependence of the SnS_2 Fermi level can also result in a more favorable position related to that of NO_2 POMO at elevated temperatures.[37,38] The temperature effect, together with its strong physical NO_2 affinity, ensures the domination of charge transfer from SnS_2 to NO_2 despite the large NO_2 gas desorption at relatively high temperatures.

The charge transfer phenomenon from the surface of 2D SnS_2 to the physisorbed NO_2 gas molecules is partially evidenced by Raman spectroscopy before and after the NO_2 exposure at 120 °C. From Figure 5a, there is no observable Raman peak shift associated with stiffening, confirming no chemical bond modification upon the physisorption of NO_2 gas molecules. The intensity of the A_{1g} Raman mode is found to be

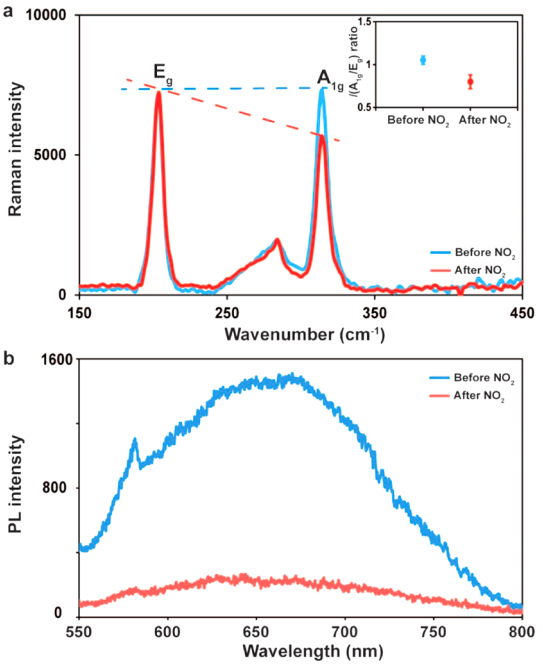

Figure 5. Physisorption based charge transfer in 2D SnS_2 flakes upon NO_2 gas exposure. (a) Raman spectra of 2D SnS_2 flakes before and after NO_2 gas exposure at 120 °C. The corresponding intensity ratio of A_{1g} and E_g modes is shown in the inset. The error bar represents the standard deviation based on the analysis of 100 samples. (b) PL spectra of 2D SnS_2 flakes before and after NO_2 gas exposure at 120 °C.

significantly reduced, while the Raman E_g mode seems to remain unchanged after the NO_2 exposure, and their intensity ratio $I(A_{1g}/E_g)$ is decreased from 1.05 to 0.8. The NO_2 adsorption may affect the equilibrium lattice parameter in SnS_2. Additionally, the NO_2 molecules on the surface act as electron acceptors, modifying the electron−phonon interaction in SnS_2. Similar to the cases of charge transfer doping observed in graphene and TMDs,[58−60] such a modification leads to the phonon self-energy renormalization and consequently weakening of the phonons, causing the intensity decrease of the A_{1g} mode that is more sensitive to the free electron density of the material.

The PL spectrum can be a good indicator in the charge transfer phenomenon, as well. As SnS_2 is an n-type semiconductor,[40] its PL peak can be theoretically decomposed into the portions of neutral exciton and the negative trion.[61] A negative trion consists of two electrons to a hole, resulting in a negatively charged exciton, while the neutral exciton is coupled to the extra electron at the Fermi level.[58] Upon the adsorption of NO_2 gas molecules, the negative trion is converted back into the neutral exciton as the free electrons are depleted from SnS_2. At the same time, the generated surface dipoles between the gas molecules and SnS_2 surface are strong enough to split the neutral excitons, leading to a significant reduction in their recombination and subsequently a strongly quenched PL (Figure 5b), which is analogous to the PL modulation

in MoS_2–WS_2 heterostacks or electrical gating of MoS_2.[61,62] In addition, it seems that such gas-molecule-induced charge transfers show no difference on the crystal polytypes of SnS_2 as the quenched degrees of the 2H and 4H PL peaks are similar.

CONCLUSIONS

We successfully developed a novel gas sensor based on 2D SnS_2 flakes with a very strong selectivity to NO_2 molecules. The 2D SnS_2 flakes were synthesized using a facile wet chemical route with a great potential for production scalability. The 2D structures of SnS_2 hexagonal planes were made of a few layers of unit cell thickness, which provided plenty of room for NO_2 molecule adsorption either on the surface or between the van der Waals spacings. The NO_2 adsorption mechanism was theoretically and experimentally shown to be dominated by physisorption with a concurrent charge transfer into 2D SnS_2 flakes that could occur at relatively low operating temperatures. Our theoretical calculations also suggested that no oxygen was involved in the NO_2 adsorption/desorption process, possibly indicating that the sensor could also operate in anaerobic environments. The best NO_2-gas-sensing performance of 2D SnS_2 was achieved at the optimum temperature of 120 °C, reaching the detection limits of <30 ppb and showing an impressive response factor of ~36 when exposed to a NO_2 concentration of 10 ppm. Excellent NO_2 selectivity was demonstrated with reference to other gas species, which had not been previously exhibited for NO_2 gas sensors that operate based on a physisorptive charge transfer mechanism. Such a unique selectivity was ascribed to the strong physical affinity of paramagnetic NO_2 gas molecules toward SnS_2 surfaces as well as the relatively favorable position between the Fermi level of SnS_2 and NO_2 POMO. Our 2D SnS_2-based NO_2 gas sensor was also highly reversible, showing excellent recovery to the baseline in contrast to 2D TMDs, such as 2D MoS_2.

The realization of the presented economical, exceptionally selective, and highly sensitive NO_2-gas-sensing platform, which operates at relatively low temperatures without the presence of oxygen, provides a feasible approach to allow high-performance NO_2 sensing for a wide range of applications in environmental monitoring, industry, clinical practices, and healthcare.

MATERIALS AND METHODS

Synthesis of 2D SnS_2 Flakes. Tin(IV) chloride ($SnCl_4 \cdot 5H_2O$, >99.9%, Sigma-Aldrich, 0.5 mM) was added to a mixture of 5 mL of oleic acid (>90.0%, Sigma-Aldrich) and 10 mL of octadecene (>90.0%, Sigma-Aldrich) in a 100 mL three-neck flask to produce the tin precursor. A standard Schlenk line was used to protect the reaction from oxygen and moisture under a flow of high-purity N_2. The mixed solution was degassed at 120 °C for 1 h to remove the moisture and the oxygen. Subsequently, the solution was heated to 280 °C within 15 min with a vigorous stir (700 rpm). Sulfide powder (1 mM) was dispersed into 5 mL of oleylamine (>90.0%, Sigma-Aldrich) to produce the sulfide precursor that was subsequently injected into the reaction system. The reaction was maintained at 280 °C for 30 min. After the solution was cooled to room temperature, the 2D SnS_2 flakes (in powder form) were collected and separated from the solution by centrifugation. The powder was further washed two times by ethanol and hexane (1/1, v/v) and finally dispersed in ethanol. The powder was stable in air without further protection for characterizations.

Morphological, Structural, and Optical Characterizations. Lateral dimensions and thicknesses of 2D SnS_2 flakes were measured using DLS (ALV fast DLS particle sizing spectrometer) and AFM (Bruker Multimode 8 with PF TUNA), respectively. Their crystal structure was characterized using XRD (Philips PANanalytical) with Cu Kα radiation at 45 kV and 40 mA, HRTEM (TEM, Tecnai F20, FEI) at an accelerating voltage of 200 kV, and Raman spectroscopy (Craic 20-30 microspectrophotometer) under the excitation wavelength of 785 nm at 1 mW power. The EDX spectrum and mapping of the flakes were carried out by scanning electron microscopy (JEOL JSM6700F) equipped with an EDX spectroscope. The optical absorption spectra of the 2D flakes were examined using a Varian Cary 500 spectrometer in dual beam mode using quartz cuvettes. PL spectroscopy was carried out on a Princeton Instruments SP2500i with a PIXIS100 ExCelon CCD camera detector using a monochromatic 532 nm laser delivering approximately 200 μW average power to the sample.

Gas Sensor Fabrication and Characterization. The transducing substrates were made of an alumina pattern with 8 pairs of IDE Pt electrodes. The spacing between each IDE pair was 200 μm. Five microliters of suspension containing 1 mg/mL of 2D SnS_2 flakes was drop-casted on the transducing substrate within the exposed area of 0.5 cm × 0.5 cm at a temperature of 50 °C. The resistance of the sensor was measured using an Agilent 34410A digital multimeter. The gas-sensing measurements were conducted in a LINKAM (Scientific Instruments) customized gas testing chamber with the capability to control the operation temperature for up to 600 °C. A computerized mass flow control multichannel gas calibration system was used to regulate the incoming gas stream at a total constant flow rate of 200 sccm to the LINKAM chamber. For the investigation of NO_2-gas-sensing performance in the humidified environment, the humidification of the gas was realized by a simple unheated bubble humidifier, in which the gas was forced down a tube into the bottom of a bottle containing 100 mL of water. The gas then escaped from the distal end of the tube under the water surface, forming bubbles, which gained humidity as they rose to the water surface. Given the relatively smaller gas flow rate (200 sccm or 0.2 L/min), the relative humidity of the incoming gas stream toward the sensor reached approximately 100%,[63,64] which was also confirmed by a commercial humidity sensor.

Theoretical Calculation on the Surface Adsorption Energy and Total Density of States. Spin-dependent hybrid DFT calculations were carried out with the Gaussian basis set *ab initio* package CRYSTAL14.[65,66] The B3LYP hybrid exchange-correlation functional was used[67] that was augmented with an empirical London-type correction to the energy in order to incorporate dispersion contributions to the overall energy. The correction term used in these calculations is the one proposed by Grimme,[68] which has been successfully used with B3LYP to calculate cohesive energies in dispersion-bonded molecular crystals.[69] For all atoms (other than Sn), a triple-ζ valence basis set, with polarization functions, was used for modeling the electrons.[70] In contrast, a fully relativistic effective core potential was used for Sn, accounting for the 28 core electrons ($1s^2 2s^2 2p^6 3s^2 3p^6 3d^{10}$) and a 411(51d) basis set for the valence electrons.[71] A periodic 3 × 3 × 1 or 5 × 5 × 1 slab of SnS_2 was used to represent the SnS_2 surface. Initially, each target gas molecule was placed ~1.5 Å from the S surface layer of SnS_2, and the molecule/slab configuration was geometry-optimized prior to calculating the molecule–slab binding energy.

Conflict of Interest: The authors declare no competing financial interest.

Acknowledgment. The authors acknowledge support from the Australian Research Council (ARC) through Discovery Project DP140100170 and the Australian National Health and Medical Research Council (NHMRC) through Development Grant 1075568. The authors would also like to acknowledge the facilities as well as scientific and technical assistance of the Australian Microscopy & Microanalysis Research Facility at the RMIT University Microscopy & Microanalysis Facility, and the Micro Nano Research Facility (MNRF) at RMIT University. This work was also supported by the Chinese National Natural Science Foundation (51172257, 61371060) and the CAS/SAFEA International Partnership Program for Creative Research Teams.

Supporting Information Available: The Supporting Information is available free of charge on the ACS Publications website at DOI: 10.1021/acsnano.5b04343.

AFM statistical analysis and DLS measurements of 2D SnS_2 flakes; XRD pattern of flakes synthesized by shorter reaction time; XPS analysis of 2D SnS_2 flakes; EDX spectrum and mapping of 2D SnS_2 flakes; Raman spectra of 2D SnS_2 flakes at different temperatures; recovery kinetics of 2D SnS_2 flakes after NO_2 gas exposure; and NO_2-gas-sensing performance of 2D SnS_2 flakes in the humidified environment (PDF)

REFERENCES AND NOTES

1. Guarnieri, M.; Balmes, J. R. Outdoor Air Pollution and Asthma. *Lancet* **2014**, *383*, 1581–1592.
2. Schwela, D. Air Pollution and Health in Urban Areas. *Rev. Environ. Health* **2000**, *15*, 13–42.
3. EPA, U.S. Air Pollution; www.epa.gov/air/nitrogenoxides/ (accessed June 30, 2015).
4. Atkinson, R. Atmospheric Chemistry of VOCs and NOx. *Atmos. Environ.* **2000**, *34*, 2063–2101.
5. Hodge, C. A. *Pollution Control in Fertilizer Production*; CRC Press: Boca Raton, FL, 1994.
6. Ou, J. Z.; Yao, C.; Rotbart, A.; Muir, J. G.; Gibson, P. R.; Kalantar-zadeh, K. Human Intestinal Gas Measurement Systems: *In Vitro* Fermentation and Gas Capsules. *Trends Biotechnol.* **2015**, *33*, 208–213.
7. Puckett, J. L.; George, S. C. Partitioned Exhaled Nitric Oxide to Non-Invasively Assess Asthma. *Respir. Physiol. Neurobiol.* **2008**, *163*, 166–177.
8. Andringa, A.-M.; Piliego, C.; Katsouras, I.; Blom, P. W. M.; Leeuw, D. M. d. NO_2 Detection and Real-Time Sensing with Field-Effect Transistors. *Chem. Mater.* **2014**, *26*, 773–785.
9. Swanson, J. J.; Watts, W. F.; Newman, R. A.; Ziebarth, R. R.; Kittelson, D. B. Simultaneous Reduction of Particulate Matter and NOx Emissions Using 4-Way Catalyzed Filtration Systems. *Environ. Sci. Technol.* **2013**, *47*, 4521–4527.
10. De Castro, A. J.; Meneses, J.; Briz, S.; López, F. Nondispersive Infrared Monitoring of NO Emissions in Exhaust Gases of Vehicles. *Rev. Sci. Instrum.* **1999**, *70*, 3156–3159.
11. Jimenez, J. L.; McRae, G. J.; Nelson, D. D.; Zahniser, M. S.; Kolb, C. E. Remote Sensing of NO and NO_2 Emissions from Heavy-Duty Diesel Trucks Using Tunable Diode Lasers. *Environ. Sci. Technol.* **2000**, *34*, 2380–2387.
12. Wang, X.-D.; Wolfbeis, O. S. Fiber-Optic Chemical Sensors and Biosensors. *Anal. Chem.* **2013**, *85*, 487–508.
13. Chang, S.-C.; Stetter, J. R. Electrochemical NO_2 Gas Sensors: Model and Mechanism for the Electroreduction of NO_2. *Electroanalysis* **1990**, *2*, 359–365.
14. Privett, B. J.; Shin, J. H.; Schoenfisch, M. H. Electrochemical Sensors. *Anal. Chem.* **2008**, *80*, 4499–4517.
15. Zhuiykov, S.; Miura, N. Development of Zirconia-Based Potentiometric NOx Sensors for Automotive and Energy Industries in the Early 21st Century: What are the Prospects for Sensors? *Sens. Actuators, B* **2007**, *121*, 639–651.
16. Afzal, A.; Cioffi, N.; Sabbatini, L.; Torsi, L. NOx Sensors based on Semiconducting Metal Oxide Nanostructures: Progress and Perspectives. *Sens. Actuators, B* **2012**, *171–172*, 25–42.
17. Fine, G. F.; Cavanagh, L. M.; Afonja, A.; Binions, R. Metal Oxide Semiconductor Gas Sensors in Environmental Monitoring. *Sensors* **2010**, *10*, 5469.
18. Wehling, T. O.; Novoselov, K. S.; Morozov, S. V.; Vdovin, E. E.; Katsnelson, M. I.; Geim, A. K.; Lichtenstein, A. I. Molecular Doping of Graphene. *Nano Lett.* **2008**, *8*, 173–177.
19. Leenaerts, O.; Partoens, B.; Peeters, F. M. Adsorption of H_2O, NH_3, CO, NO_2, and NO on Graphene: A First-Principles Study. *Phys. Rev. B: Condens. Matter Mater. Phys.* **2008**, *77*, 125416.
20. Hu, T.; Gerber, I. C. Theoretical Study of the Interaction of Electron Donor and Acceptor Molecules with Graphene. *J. Phys. Chem. C* **2013**, *117*, 2411–2420.
21. Llobet, E. Gas Sensors Using Carbon Nanomaterials: A Review. *Sens. Actuators, B* **2013**, *179*, 32–45.
22. Iqbal, N.; Afzal, A.; Cioffi, N.; Sabbatini, L.; Torsi, L. NOx Sensing One- and Two-Dimensional Carbon Nanostructures and Nanohybrids: Progress and Perspectives. *Sens. Actuators, B* **2013**, *181*, 9–21.
23. Li, H.; Wu, J.; Qi, X.; He, Q.; Liusman, C.; Lu, G.; Zhou, X.; Zhang, H. Graphene Oxide Scrolls on Hydrophobic Substrates Fabricated by Molecular Combing and Their Application in Gas Sensing. *Small* **2013**, *9*, 382–386.
24. He, Q.; Wu, S.; Yin, Z.; Zhang, H. Graphene-based Electronic Sensors. *Chem. Sci.* **2012**, *3*, 1764–1772.
25. Schedin, F.; Geim, A. K.; Morozov, S. V.; Hill, E. W.; Blake, P.; Katsnelson, M. I.; Novoselov, K. S. Detection of Individual Gas Molecules Adsorbed on Graphene. *Nat. Mater.* **2007**, *6*, 652–655.
26. Cho, B.; Hahm, M. G.; Choi, M.; Yoon, J.; Kim, A. R.; Lee, Y.-J.; Park, S.-G.; Kwon, J.-D.; Kim, C. S.; Song, M.; et al. Charge-Transfer-Based Gas Sensing Using Atomic-Layer MoS_2. *Sci. Rep.* **2015**, *5*, 8052.
27. Late, D. J.; Huang, Y.-K.; Liu, B.; Acharya, J.; Shirodkar, S. N.; Luo, J.; Yan, A.; Charles, D.; Waghmare, U. V.; Dravid, V. P.; et al. Sensing Behavior of Atomically Thin-Layered MoS_2 Transistors. *ACS Nano* **2013**, *7*, 4879–4891.
28. Donarelli, M.; Prezioso, S.; Perrozzi, F.; Bisti, F.; Nardone, M.; Giancaterini, L.; Cantalini, C.; Ottaviano, L. Response to NO_2 and Other Gases of Resistive Chemically Exfoliated MoS_2-Based Gas Sensors. *Sens. Actuators, B* **2015**, *207*, 602–613.
29. He, Q.; Zeng, Z.; Yin, Z.; Li, H.; Wu, S.; Huang, X.; Zhang, H. Fabrication of Flexible MoS_2 Thin-Film Transistor Arrays for Practical Gas-Sensing Applications. *Small* **2012**, *8*, 2994–2999.
30. Li, H.; Yin, Z.; He, Q.; Li, H.; Huang, X.; Lu, G.; Fam, D. W. H.; Tok, A. I. Y.; Zhang, Q.; Zhang, H. Fabrication of Single- and Multilayer MoS_2 Film-Based Field-Effect Transistors for Sensing NO at Room Temperature. *Small* **2012**, *8*, 63–67.
31. Abbas, A. N.; Liu, B.; Chen, L.; Ma, Y.; Cong, S.; Aroonyadet, N.; Köpf, M.; Nilges, T.; Zhou, C. Black Phosphorus Gas Sensors. *ACS Nano* **2015**, *9*, 5618–5624.
32. Kou, L.; Frauenheim, T.; Chen, C. Phosphorene as a Superior Gas Sensor: Selective Adsorption and Distinct *I–V* Response. *J. Phys. Chem. Lett.* **2014**, *5*, 2675–2681.
33. Julien, C.; Eddrief, M.; Samaras, I.; Balkanski, M. Optical and Electrical Characterizations of SnSe, SnS_2 and $SnSe_2$ Single Crystals. *Mater. Sci. Eng., B* **1992**, *15*, 70–72.
34. Chhowalla, M.; Shin, H. S.; Eda, G.; Li, L. J.; Loh, K. P.; Zhang, H. The Chemistry of Two-Dimensional Layered Transition Metal Dichalcogenide Nanosheets. *Nat. Chem.* **2013**, *5*, 263–275.
35. Varrla, E.; Backes, C.; Paton, K. R.; Harvey, A.; Gholamvand, Z.; McCauley, J.; Coleman, J. N. Large-Scale Production of Size-Controlled MoS_2 Nanosheets by Shear Exfoliation. *Chem. Mater.* **2015**, *27*, 1129–1139.
36. Xu, Y.; Schoonen, M. A. A. The Absolute Energy Positions of Conduction and Valence Bands of Selected Semiconducting Minerals. *Am. Mineral.* **2000**, *85*, 543–556.
37. Patil, S. G.; Tredgold, R. H. Electrical and Photoconductive Properties of SnS_2 Crystals. *J. Phys. D: Appl. Phys.* **1971**, *4*, 718.
38. El-Mahalawy, S. H.; Evans, B. L. Temperature Dependence of the Electrical Conductivity and Hall Coefficient in

2H-MoS_2, $MoSe_2$, WSe_2, and $MoTe_2$. *Phys. Status Solidi B* **1977**, *79*, 713–722.
39. Huang, Y.; Sutter, E.; Sadowski, J. T.; Cotlet, M.; Monti, O. L. A.; Racke, D. A.; Neupane, M. R.; Wickramaratne, D.; Lake, R. K.; Parkinson, B. A.; et al. Tin Disulfide—An Emerging Layered Metal Dichalcogenide Semiconductor: Materials Properties and Device Characteristics. *ACS Nano* **2014**, *8*, 10743–10755.
40. Ahn, J.-H.; Lee, M.-J.; Heo, H.; Sung, J. H.; Kim, K.; Hwang, H.; Jo, M.-H. Deterministic Two-Dimensional Polymorphism Growth of Hexagonal *n*-Type SnS_2 and Orthorhombic *p*-Type SnS Crystals. *Nano Lett.* **2015**, *15*, 3703–3708.
41. Su, G.; Hadjiev, V. G.; Loya, P. E.; Zhang, J.; Lei, S.; Maharjan, S.; Dong, P.; Ajayan, P.; Lou, J.; Peng, H. Chemical Vapor Deposition of Thin Crystals of Layered Semiconductor SnS_2 for Fast Photodetection Application. *Nano Lett.* **2015**, *15*, 506–513.
42. Du, Y.; Yin, Z.; Rui, X.; Zeng, Z.; Wu, X.-J.; Liu, J.; Zhu, Y.; Zhu, J.; Huang, X.; Yan, Q.; et al. A Facile, Relative Green, and Inexpensive Synthetic Approach toward Large-Scale Production of SnS_2 Nanoplates for High-Performance Lithium-Ion Batteries. *Nanoscale* **2013**, *5*, 1456–1459.
43. Kim, T.-J.; Kim, C.; Son, D.; Choi, M.; Park, B. Novel SnS_2-Nanosheet Anodes for Lithium-Ion Batteries. *J. Power Sources* **2007**, *167*, 529–535.
44. Seo, J.-w.; Jang, J.-t.; Park, S.-w.; Kim, C.; Park, B.; Cheon, J. Two-Dimensional SnS_2 Nanoplates with Extraordinary High Discharge Capacity for Lithium Ion Batteries. *Adv. Mater.* **2008**, *20*, 4269–4273.
45. Zhang, Y. C.; Du, Z. N.; Li, S. Y.; Zhang, M. Novel Synthesis and High Visible Light Photocatalytic Activity of SnS_2 Nanoflakes from $SnCl_2 \cdot 2H_2O$ and S Powders. *Appl. Catal., B* **2010**, *95*, 153–159.
46. Björkman, T.; Gulans, A.; Krasheninnikov, A. V.; Nieminen, R. M. Van Der Waals Bonding in Layered Compounds from Advanced Density-Functional First-Principles Calculations. *Phys. Rev. Lett.* **2012**, *108*, 235502.
47. Smith, A. J.; Meek, P. E.; Liang, W. Y. Raman Scattering Studies of SnS_2 and $SnSe_2$. *J. Phys. C: Solid State Phys.* **1977**, *10*, 1321.
48. Chandrasekhar, H. R.; Humphreys, R. G.; Zwick, U.; Cardona, M. Infrared and Raman Spectra of the IV-VI Compounds SnS and SnSe. *Phys. Rev. B* **1977**, *15*, 2177–2183.
49. Price, L. S.; Parkin, I. P.; Hardy, A. M. E.; Clark, R. J. H.; Hibbert, T. G.; Molloy, K. C. Atmospheric Pressure Chemical Vapor Deposition of Tin Sulfides (SnS, Sn_2S_3, and SnS_2) on Glass. *Chem. Mater.* **1999**, *11*, 1792–1799.
50. Seminovski, Y.; Palacios, P.; Wahnón, P. Effect of Van Der Waals Interaction on the Properties of SnS_2 Layered Semiconductor. *Thin Solid Films* **2013**, *535*, 387–389.
51. Domingo, G.; Itoga, R. S.; Kannewurf, C. R. Fundamental Optical Absorption in SnS_2 and $SnSe_2$. *Phys. Rev.* **1966**, *143*, 536–541.
52. Faglia, G.; Baratto, C.; Sberveglieri, G.; Zha, M.; Zappettini, A. Adsorption Effects of NO_2 at ppm Level on Visible Photoluminescence Response of SnO_2 Nanobelts. *Appl. Phys. Lett.* **2005**, *86*, 011923.
53. Shibata, T.; Kambe, N.; Muranushi, Y.; Miura, T.; Kishi, T. Optical Characterisation of Single Crystal 2H-SnS_2 Synthesised by the Chemical Vapour Transport Method at Low Temperatures. *J. Phys. D: Appl. Phys.* **1990**, *23*, 719.
54. Deshpande, N. G.; Sagade, A. A.; Gudage, Y. G.; Lokhande, C. D.; Sharma, R. Growth and Characterization of Tin Disulfide (SnS_2) Thin Film Deposited by Successive Ionic Layer Adsorption and Reaction (SILAR) Technique. *J. Alloys Compd.* **2007**, *436*, 421–426.
55. NIOSH. *NIOSH Pocket Guide to Chemical Hazards*; http://www.cdc.gov/niosh/npg/npgd0454.html (accessed September, 23, **2015**).
56. Shi, W.; Huo, L.; Wang, H.; Zhang, H.; Yang, J.; Wei, P. Hydrothermal Growth and Gas Sensing Property of Flower-Shaped SnS_2 Nanostructures. *Nanotechnology* **2006**, *17*, 2918.
57. Zhao, S.; Xue, J.; Kang, W. Gas Adsorption on MoS_2 Monolayer from First-Principles Calculations. *Chem. Phys. Lett.* **2014**, *595–596*, 35–42.
58. Liu, J.; Li, Q.; Zou, Y.; Qian, Q.; Jin, Y.; Li, G.; Jiang, K.; Fan, S. The Dependence of Graphene Raman D-Band on Carrier Density. *Nano Lett.* **2013**, *13*, 6170–6175.
59. Voggu, R.; Das, B.; Rout, C. S.; Rao, C. N. R. Effects of Charge Transfer Interaction of Graphene with Electron Donor and Acceptor Molecules Examined Using Raman Spectroscopy and Cognate Techniques. *J. Phys.: Condens. Matter* **2008**, *20*, 472204.
60. Shi, Y.; Huang, J.-K.; Jin, L.; Hsu, Y.-T.; Yu, S. F.; Li, L.-J.; Yang, H. Y. Selective Decoration of Au Nanoparticles on Monolayer MoS_2 Single Crystals. *Sci. Rep.* **2013**, *3*, 1839.
61. Yuan, J.; Najmaei, S.; Zhang, Z.; Zhang, J.; Lei, S.; Ajayan, P. M.; Yakobson, B. I.; Lou, J. Photoluminescence Quenching and Charge Transfer in Artificial Heterostacks of Monolayer Transition Metal Dichalcogenides and Few-Layer Black Phosphorus. *ACS Nano* **2015**, *9*, 555–563.
62. Newaz, A. K. M.; Prasai, D.; Ziegler, J. I.; Caudel, D.; Robinson, S.; Haglund, R. F., Jr.; Bolotin, K. I. Electrical Control of Optical Properties of Monolayer MoS_2. *Solid State Commun.* **2013**, *155*, 49–52.
63. Al Ashry, H. S.; Modrykamien, A. M. Humidification during Mechanical Ventilation in the Adult Patient. *BioMed Res. Int.* **2014**, *2014*, 1–12.
64. Kacmarek, R. M.; Stoller, J. K.; Heuer, A. *Egan's Fundamentals of Respiratory Care*; Elsevier: Amsterdam, 2013.
65. Dovesi, R.; Orlando, R.; Erba, A.; Zicovich-Wilson, C. M.; Civalleri, B.; Casassa, S.; Maschio, L.; Ferrabone, M.; De La Pierre, M.; D'Arco, P.; et al. CRYSTAL14: A Program for the *Ab Initio* Investigation of Crystalline Solids. *Int. J. Quantum Chem.* **2014**, *114*, 1287–1317.
66. Dovesi, R.; Saunders, V. R.; Roetti, C.; Orlando, R.; Zicovich-Wilson, C. M.; Pascale, F.; Civalleri, B.; Doll, K.; Harrison, N. M.; Bush, I. J.; et al. *CRYSTAL14 User's Manual*; University of Torino: Torino, Italy, 2014.
67. Becke, A. D. Density-Functional Thermochemistry. III. The Role of Exact Exchange. *J. Chem. Phys.* **1993**, *98*, 5648–5652.
68. Grimme, S. Semiempirical GGA-Type Density Functional Constructed with A Long-Range Dispersion Correction. *J. Comput. Chem.* **2006**, *27*, 1787–1799.
69. Civalleri, B.; Zicovich-Wilson, C. M.; Valenzano, L.; Ugliengo, P. B3LYP Augmented with An Empirical Dispersion Term (B3LYP-D*) as Applied to Molecular Crystals. *CrystEngComm* **2008**, *10*, 405–410.
70. Peintinger, M. F.; Oliveira, D. V.; Bredow, T. Consistent Gaussian Basis Sets of Triple-Zeta Valence with Polarization Quality for Solid-State Calculations. *J. Comput. Chem.* **2013**, *34*, 451–459.
71. Crystal-Basis Sets Library. http://www.crystal.unito.it/basis-sets.php.